# Deformation and failure mechanisms of granular soil around pressurised shallow cavities

F. PATINO-RAMIREZ* F. ANSELMUCCI ‡ E. ANDÒ ‡ G. VIGGIANI ‡ B. CAICEDO † C. ARSON *

The deformation patterns and failure mechanisms of pressurised cavities at shallow depth are of relevance to many geotechnical applications, including tunneling and horizontal directional drilling. In this paper, we present an experimental study of a reduced-scale pressurised cavity under geostatic stress, in order to measure the effect of cavity length, vertical stress and soil density on soil deformation and failure. x-ray computed tomography is used to acquire images of the system at key stages of the cavity inflation process. A closed shaped failure region developed around the cavities, beyond which, shear planes of elliptic paraboloid shape formed, extending from the bottom of the cavities all the way to the free surface. The plane strain assumption did not hold beyond the central portion of the longest cavity tested (L = 6D). The volumetric strain and porosity changes inside the shear bands showed significant dilation in dense specimens, but contraction in loose specimens. The average orientation and the thickness of the shear bands were in agreement with those found in the literature for passive arching mechanisms (anchoring). The orientation of the principal strains around the cavity follows catenary shapes, similar to those displayed in active trapdoor mechanisms.

KEYWORDS: cavity expansion, x-ray tomography, image analysis, deformation, failure

## INTRODUCTION

The cavity expansion theory has been used for a wide range of applications in geomechanics, from in-situ testing (Mair & Wood, 1987; Li *et al.*, 2016) to extraction wells and tunnel design (Atkinson & Potts, 1977; Wong *et al.*, 2012). For instance, the pressuremeter test (Wood, 1990), the cone penetration test (Salgado *et al.*, 1997; Russell & Khalili, 2006) and the dilatometer test (Zhou *et al.*, 2016) can be modelled as expanding pressurised cavities. Similarly, extraction wells, relevant to hydraulic fracturing and geothermal foundations, involve vertical cavities subjected to changes in internal pressure and/or diameter. Similarly, horizontal cavities such as deep tunnels, micro-tunnels and horizontal directional drills can be considered (to some extent) as pressurised (or de-pressurised) cavities (Chapman *et al.*, 2018). In the present study, we focus on the problem of shallow, horizontal cavities embedded in granular media (sand) and characterise the failure mechanism that develops during their pressurisation. This problem is particularly relevant to Horizontal Directional Drilling (HDD), which involves the circulation of pressurised drilling fluid along the cavity body; the borehole stability is then controlled by the maximum pressure that can be applied to the cavity before it fails (Bennett & Ariaratnam, 2017).

Classic cavity expansion theories were developed for infinite domains, assuming plane strain, stress/strain coaxiality and absence of shear at the cavity wall. Stress distributions around holes were initially calculated within the theory of elasticity (Timoshenko & Goodier, 1951; Muskhelishvili, 1977) and solutions were found for pressurised cavities by means of the superposition principle. Extension to plasticity (Hill, 1950) brings important mathematical challenges, especially in the absence of symmetries that reduce the dimensionality of the problem. An important tool used to find closed-form solutions to cavity expansion problems under anisotropic far-field stresses is complex mapping, as described by Nehari (1952). Analytical solutions depend on the choice of constitutive model, drained vs. undrained conditions, cavity shape and far-field stresses (isotropic vs. anisotropic). A comprehensive review of cavity expansion theories applied to geomechanics is available in (Yu, 2000).

Cavity expansion theories developed for an infinite domain are only applicable when the size of the cavity is relatively small compared to the dimensions of the domain it is embedded in. However, for a shallow and horizontal cavity this assumption does not necessarily hold true, since the presence of a free surface and the gradient of stresses around the cavity become significant, and the geostatic stress field can no longer be modelled as an isotropic or biaxial state. Still, most models proposed to assess borehole stability still make use of cavity expansion theories (Neher, 2013), including the Standard Guide for horizontal directional drilling from the American Society for Testing and Materials: ASTM - F1962 - 11 (ASTM, 2011) and the current Good Practices Guidelines for HDD from the NASTT (North American Society For Trenchless Technology) (Bennett & Ariaratnam, 2017) which recommend a model of cylindrical cavity expansion in an infinite domain called the the Delft equation (Keulen, 2001) to assess the stability of the borehole. The failure of such shallow cavities is controlled by tensile stresses (developed at the crown of the cavity) in the case of cohesive materials and by shear stresses (which originate 'blow-out') for cohesion-less media Lan & Moore (2017). Regardless of the nature of the soil, the use of cavity expansion theories (such as the Delft equation) results in an overestimation of the maximum pressure that can be safely imposed to the cavity as shown in (Kennedy *et al.*, 2006; Xia & Moore, 2006; Lan & Moore, 2018) for purely cohesive materials and in (Lan & Moore, 2020) for frictional soils. For instance, the Delft equation overestimates the maximum pressure by by 90%–170%.

Experimental evidence suggests that the shear mechanism that controls the failure of shallow cavities is characterised by the development of shear bands that originate from the waist of the cavity and extend to the free surface. Recently, Lan & Moore (2020) modeled blow-out for HDD and found that mud flow followed (possibly) curved shear planes oriented at

* Department of Civil and Environmental engineering, Georgia Institute of Technology, Atlanta, GA, 30332, USA. † Civil and Environmental Engineering Department, Universidad de los Andes, Bogotá, Colombia. ‡ Univ. Grenoble Alpes, CNRS, Grenoble INP, 3SR, F-38000 Grenoble, France

a certain angle from the vertical. These findings suggest that the presence of a free surface close to the expanding cavity changes the failure mechanism of the soil, which transitions from a circular/elliptical plastic region around the cavity (as predicted from cavity expansion), to a mechanism dominated by the development of shear planes starting from the cavity and reaching the free surface. Such failure mechanism resembles the well known passive trapdoor mechanism, first studied by Karl Terzaghi Terzaghi *et al.* (1996) and later documented in a number of studies, e.g. (Evans, 1984; Tien, 1996) and more recently by Costa *et al.* (2009) around pipes in active trapdoor experiments and by anchoring mechanisms as shown by Mallett *et al.* (2018). These observations suggest that the failure mechanism of shallow pressurised cavities is driven by passive arching. The phenomenon of arching has been documented in the literature that reports settlements and de-pressurisation caused by excavation Ji *et al.* (2018) and in studies that investigate tunnel face stability Lee *et al.* (2006); Zou *et al.* (2019).

In this paper, we analyse the failure mechanisms around a shallow cylindrical pressurised cavity embedded in dry sand. A reduced-scale model was tested under geostatic stress conditions and imaged with an x-ray micro-computed tomographer during pressurisation, depressurisation and re-pressurisation to failure. Soil failure could not be explained by the cavity expansion theory and was instead dominated by passive anchoring. We analysed the influence of vertical stress, soil density and cavity length on cavity deformation, soil porosity changes and displacement/strain fields around the cavity. We first describe our experimental protocols along with the materials tested. Second, we present our image analyses and we interpret the cavity deformation and the soil strain field. Third, we discuss the failure mechanisms and we evaluate the plane strain assumption. Lastly, we summarise our conclusions.

## MATERIALS AND METHODS

### *Experimental Setup*

The experimental setup is shown in Fig 1. A cylindrical container held the soil specimen and applied the surcharge vertical stress ($\sigma_v$). The soil specimen was 10 cm in height and diameter. The inflatable probe that was used to model the pressurised cavity was placed horizontally inside the soil. A syringe pump was connected to the probe for pressurisation. All the components were made of plastic, since metals cause significant attenuation of the x-rays.

We use a Cartesian coordinate system in which the Z-axis (in the vertical direction) is oriented along the axis of the cylindrical container. The datum is placed at the top of the soil specimen and the Z axis points downwards, i.e. Z increased with depth. The Y-axis is oriented along the axis of the (initially) cylindrical probe/cavity, with the origin at the end of the probe furthest away from the pump. The X-axis is normal to the Y and Z axes, as shown in Fig 1. From this point onward, we will refer to three cross-sections, all passing through the mid-point of the device along the Y axis. The cross-section along the XZ plane, in which the device appears as a circle/ellipse, will be referred as the front view. The cross-section along the YZ plane will be referred as the side view, and the section along the XY plane is referred as the top view.

The soil container is made of a plexiglass cylinder with an internal diameter of 10 cm, a wall thickness of 1 cm and a height of 40 cm. The loading system fastened at the top of the container consists of a pneumatic actuator connected to a plastic piston and a neoprene membrane that transferred the load to the top of the soil specimen. Note that the side wall was not treated to further control the load transfer. The pressure applied by the actuator was regulated using a manometer connected to a line of pressurised air. The use of a relatively long plastic piston to transfer the load was necessary, to guarantee that none of the metallic parts of the pneumatic actuator fell within the region of the set up being scanned. Three different vertical pressures were applied in the experimental campaign: $\sigma_{V1} = 3.5 kPa$, $\sigma_{V2} = 6 kPa$ and $\sigma_{V3} = 8 kPa$. For the lowest of these vertical stresses ($\sigma_{V1}$) weights were used instead of the pneumatic actuator (the remainder of the loading system was unchanged). Higher pressures were used in preliminary tests but discarded since they did not allow yielding of the cavity at the range of cavity pressures tested ($< 200 kPa$). No significant lateral wall deflection was observed from the acquired images after application of the vertical load.

We used HN31 sand (Andò, 2013), a fine, angular and uniformly graded sand with particle sizes between $0.16 mm$ and $0.63 mm$, a mean particle size ($d_{50}$) of $0.34 mm$, and a coefficient of uniformity of $1.70$. The specific gravity (Gs) of the material was 2.65. The minimum and maximum unit weights of the material were $13.24$ and $15.99 kN/m^3$ (Desrues & Viggiani, 2004; Andò, 2013), which correspond to void ratios of $1.00$ and $0.66$ or porosities of $50.0\%$ and $33.7\%$ respectively, and will be used as the bounds to define the relative density ($D_R$). The specimens were dry pluviated in two layers using a funnel with an opening diameter of $1.2 cm$. The first layer extended from the bottom to a height of $5 cm$, where the probe was placed horizontally at the center of the cylinder. The second layer was formed to reach a total height of $10 cm$. Two different elevations of 5 and $50 mm$ were used to achieve relative densities $D_R$ of $22\%$ ("loose specimens") and $65\%$ ("dense specimens") respectively.

The probes were $10 mm$ in diameter and were similar to a single chamber Menard pressuremeter. Holes were drilled at regular spacings in an acrylic cylinder of $9.52 mm$ in diameter that was wrapped within a thin latex membrane with a thickness of approximately $0.25 mm$. The membrane was clamped at the ends of the cylinder with o-rings and custom made gaskets. One of the ends of the probe was connected with a tube fitting to a relatively rigid polyurethane tubing connected to the inflation setup. The other end was closed tightly using a plastic screw to avoid leaks. We tested probes of three different lengths: 20, 40 and $60 mm$, corresponding to 2, 4 and 6 times the probe diameter.

The inflation setup consisted of a syringe pump set at a constant rate of $0.2 cm^3/min$. Probes were inflated with water, which can be assumed incompressible at the range of pressures tested (below $200 kPa$). A high-grade syringe pump was connected to the device using polyurethane tubing. The length of the tubing was kept to a minimum in order to minimise volume and pressure loss. A pressure transducer (Omega PX26) with a capacity of $200 kPa$ (accuracy $\pm 1\%$) was connected to the pressure line, using a T-shape, to monitor the internal pressure of the system, as shown in Fig 1.

### *Boundary and grain size effects*

The sample size used in this study was maximised up to the limit set by the spatial resolution and size of the tomographer, yet it was relatively small per geotechnical laboratory testing standards. As such, the experimental setup may be affected by boundary effects (e.g. influence of the container walls) and/or grain size effects (e.g. influence of grains that are large compared to the probe).

The soil sample had a diameter of $100 mm$ ($10 cm$) while the inflatable probe had a diameter of $10 mm$ for a
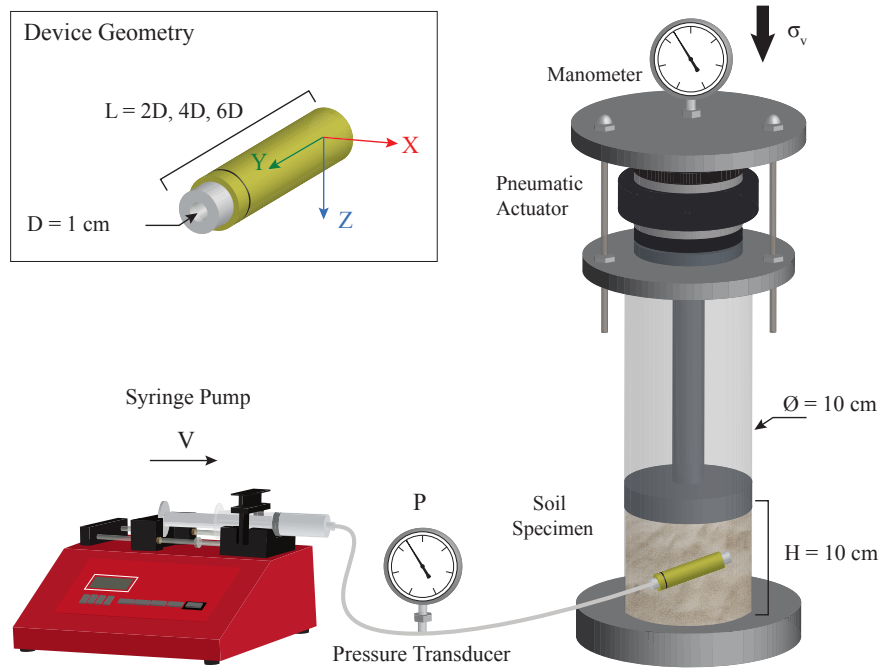
**Fig. 1. Experimental Setup. Soil specimen placed inside scanning region. Pressure and volume monitored during expansion steps and scanning.**

ratio of 10; however, considering the length of the probes ($20, 40 and 60mm$), the distance between the probe ends and the container was reduced, specially for the longest cavities where the shortest distance between the probe cap and the container was slightly under $20mm$. Manufacturing probes with a smaller diameter proved unfeasible due to the limited availability of small-size plastic components that could hold the maximum internal pressure of $200kPa$.

In an attempt to quantify the presence of boundary effects, we measured the change in porosity adjacent to the container wall. Ideally, the container would be large enough so that the influence of the expansion of the probe does not reach the neighborhood of the container walls, therefore having a null change in porosity. The porosity was measured for cylindrical shells with a thickness of $5mm$ and varying outside diameter from $5mm$ (center of container) to $50mm$ (adjacent to container wall).

Results from Fig 2 show that the largest change in porosity adjacent to the container was indeed observed in the tests with the longest cavities (L=6D) with a maximum average change of porosity of 2.1%. For shorter cavities, the change of porosity was below 1.4%. Most of the observations in the following sections focus on the cross-section orthogonal to the cavity axis through the cavity center (front view), at the point that is the farthest away from the container walls. Still, the effect of the container must be kept in mind when making further interpretations of the results.

The use of smaller expandable probes minimizes the boundary effects from the container but can trigger grain size effects if the grains are relatively large compared to the structure (probe) size. Previous studies on buried structures or piles undergoing lateral load suggest that there are no grain effects is the size of the structure is 44 to 48 times greater than the $d_{50}$ of the material (Garnier *et al.*, 2007). In this study, the size ratio is 29.4, indicating that some grain effect could be present. However, the relationships between the size of the structure and the maximum grain size ($B/d_{max}$) proposed in (Biarez & Hicher, 1994) and (Caicedo, 2018) ($B/d_{max} < 10$

or $B/d_{max} < 15$ respectively) allow to conclude that in the tests presented in this study ($B = 10mm$, $d_{max} = 0.63mm$ and $B/d_{max} = 15.9$) the stress distribution error due to grain size is lower than 10%.

*Testing procedure*

Before every test, each probe was purged to make sure that no air bubbles were trapped inside. Then, following previous recommendations (Mair & Wood, 1987), two different calibration steps were performed before each test. First, the probe was hung vertically and inflated up to three times its initial volume. The obtained pressure vs. volume response of the probe corresponds to the resistance of the membrane and the tubing system, which we later deducted from the response of the expansion inside the soil specimen. Second, we measured the compliance of the system, e.g. the deformation of the tubing assembly. The probes were placed inside a tight fitting metal tube (considered rigid at the range of pressures tested) and then pressurised until a maximum pressure of 200 kPa was reached. Fig 3 shows typical calibration curves. Incidentally, measuring the compliance of the system helped identify leaks and trapped air bubbles.

After each specimen was prepared, the container was placed in the x-ray scanner and scanned three times. The first baseline step scanned the specimen before the inflation of the probe. Next, the probe was inflated until the pressure reached a peak or stabilised, and the inflation stopped. A second scan was taken then. Lastly, the device was further inflated until its volume reached three times its initial volume, and then a third scan was performed. We conducted a total of 13 tests, 12 of them combining two relative densities ($D_R$ 22% and 65%), three probe lengths (2, 4 and 6 times the probe diameter) and two surcharge pressures ($\sigma_{V1} = 3.5kPa$ and $\sigma_{V2} = 6kPa$). A last test considered specimen with $D_R$ 22%, probe length $6D$ and vertical surcharge $\sigma_{V3} = 8kPa$.
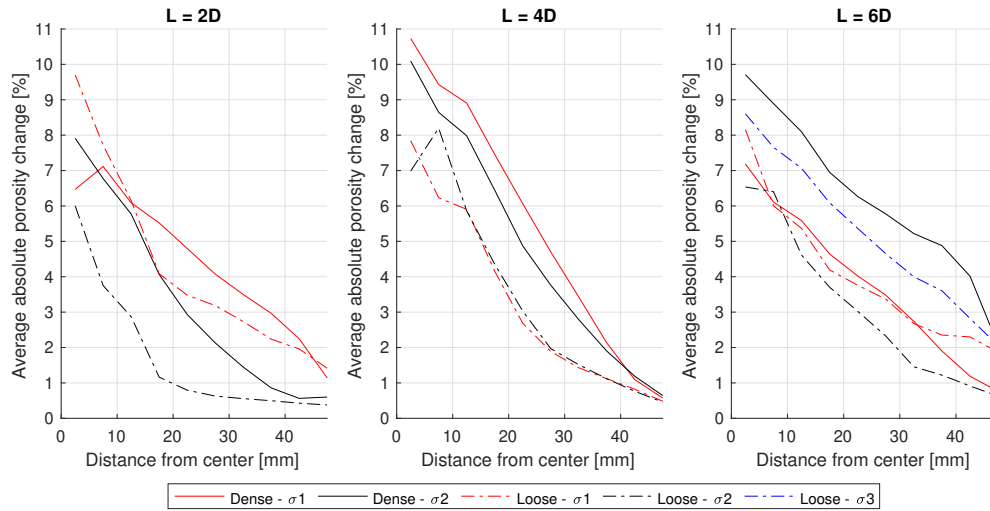
**Fig. 2. Average change in porosity after device expansion. Porosity measured in** $5mm$ **cylindrical shells from the center to the border of the sample container.**
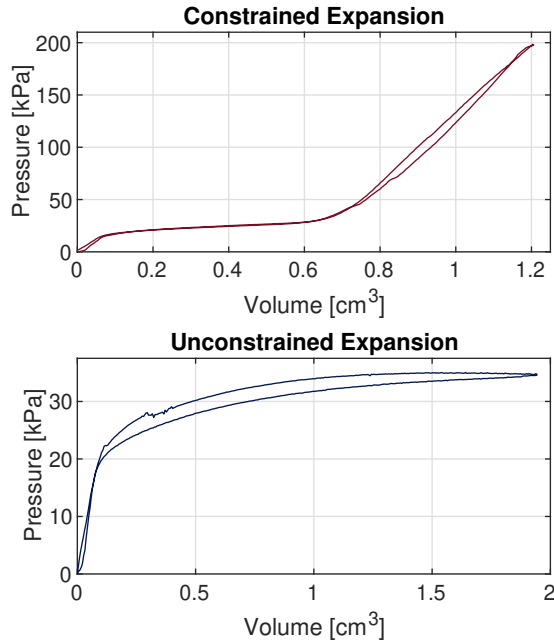


**Fig. 3. Typical probe calibration curves. "Dense" sand, probe with L = 2D and vertical stress** $\sigma_{V1} = 3.5kPa$

*Image acquisition*

The scanning volume was a prism with a height of $90mm$ and a cross section of $119mm$ by $119mm$. The resolution of the acquired images was controlled by the voxel size, which we set as $70\mu m$ (approximately one fifth of $d_{50}$). The scanned volume was then cropped to remove the container and the bottom $20mm$ of the sample, since preliminary tests showed that they were not affected by the expansion of the probes. After cropping the acquired images, we obtained stacks of 1430-by-1430-by-1000 voxels, corresponding to a volume of $100 - by - 100 - by - 70mm$. The present section includes the strictly necessary details about the process of image acquisition using x-ray computed tomography (CT-scanning). For further details and a comprehensive description of the Digital volume correlation (DVC) procedures, we refer the readers to (Stamati, 2020).

*Image Analysis*

**Cavity Deformation**

Images were segmented to analyse the deformation of the probe (or cavity). The grey value that best separated the probe from the soil grains was used as a threshold to binarise the images and exclude the probe domain from the soil deformation analysis. The binarisation was performed sequentially, starting from the horizontal slice that passes through the center of the probe (of known location). We identified the horizontal cross section of the probe as the largest connected component after binarisation. Then, the raw cross section was smoothed by eroding and dilating its contour, with a structuring element of 10 voxels in radius (two times the mean grain size). Then, two independent loops were run to sequentially add horizontal cross sections to the segmented 3D cavity volume towards the top and bottom of the specimen. In order to ensure continuity of the segmented volume, the connected component of a subsequent slice must share at least one voxel location with the previous slice. The cross sections of the cavity reduced in size as the distance from the middle of the device increased, until the cavity footprint vanished, at which point, the segmentation was completed. Then, the centroid, area, major and minor axes of the convex (ellipsoidal) cross-sections of the cavity were stored for further analysis.

**Soil Deformation**

Before analysing soil deformation, corners of the cylindrical container were masked together with the segmented cavity volume. Soil displacement fields were computed using the open-source, python package SPAM (Stamati *et al.*, 2020). The local DVC algorithm splits the 3D image into sub-volumes in the reference configuration, and for each subvolume iteratively solves for the linear transformation function that offers the best match with the greyscale texture in the deformed configuration. The result is thus a transformation function for each subvolume which includes a 3D displacement vector whose accuracy is well below the pixel. Sub-volumes are centered around a given node, and are spaced along the three dimensions of the image. The size of the sub-volumes is controlled by the window size (WS). We set the WS as 33 voxels (about 6.4 times the average grain width - $d_{50}$), while the distance between nodes (known as node spacing) was 24 voxels (4.8 times $d_{50}$) in all

three directions, meaning that there was some overlapping of subvolumes.

The obtained displacement fields had convergence rates above 98%, i.e. less than 2% of the nodes could not be correlated between consecutive images. The strain fields were computed using Q8 shape functions and the displacement gradient tensor (**F**), which is a measure of the local displacement variations. We used a finite strain formulation given the significant distortion of the soil matrix. Local measurements of porosity were performed on every image. The resolution of our images did not allow a binary segmentation between grain and void phases and therefore a linear greyscale calibration (non-binary) classification was used. The calibration between grey values and porosity was performed for each test (essentially the identification of the grains and void greyvalues), allowing porosity to be computed on appropriately defined subvolumes. Similar to the displacement and strain fields calculation, the voxels outside of the container and inside of the cavity were excluded from the analysis.

## Porosity Measurement

The total volume and mass of the specimen were measured prior to testing. Assuming weightless air and the known specific gravity (Gs) of the sand ($G_s 02.65$) the global porosity of the samples was calculated. Then, from the masked images (which contain only the soil sample) a binary threshold was found to match the porosity of the image to the actual measured porosity of the sample. The binary images (in which each voxel is either void or grain) were then split into cubic windows of analysis ($12^3$ voxels), and for each window, the local porosity was measured.

## RESULTS

### Cavity response

#### Pressure vs. Volume response

The pressure - volume response of the cavities was monitored during the tests and was corrected to account for the compliance and resistance of the membrane around the probe. Figure 4 shows the resulting response of the cavities for the different probe lengths, soil densities and surcharge vertical stresses tested. The observed loss of pressure at constant volume (vertical lines in the cavity response) corresponds to the moment at which the inflation step was stopped to acquire the first tomography. The drops in pressure corresponds to the scanning periods, which lasted about an hour.

The two longer cavities (L = 4D, 6D) exhibited similar pressure-volume responses, while the shorter cavities showed significantly higher pressures as a result of the increase in volume. Dense soils exhibited a stiffer response that reaches a peak resistance, and decreases afterwards, typical of dilative materials. Conversely, loose specimens showed a more ductile response, with an asymptotic behavior, typical of contractive specimens. In the same way, a higher vertical surcharge pressure resulted in higher maximum resistance of the specimen.

A normalized multivariate linear regression was used to quantify the correlation between the test variables (cavity length, soil density and vertical surcharge) and the peak cavity resistance (maximum pressure value recorded during the test). Since the test variables were normalized (their values scaled between 0 and 1), the coefficients of the regression show the relationships, direct (+) or inverse (-), and their relative influence (magnitude) on the cavity response. The linear regression obtained is shown in Eq. 1.

$$P = 0.66\sigma_v + 0.58D_R - 0.49L \qquad R^2 = 0.82 \qquad (1)$$

The regression in Eq 1 shows that 82% of the variability of the peak cavity response can be explained with a linear combination of the tested variables. The largest influence in the soil resistance ($P$) comes from the surcharge vertical stress ($\sigma_v$), followed by the relative density of the soil ($D_R$), both of which are positively correlated to $P$. Conversely, the device length ($L$) is negatively correlated to the peak response, meaning that shorter devices yield a higher peak resistance.

## Cavity deformation

The anisotropic stress conditions around the cavity cause a non-homogeneous deformation of the cavity during its expansion. To characterise the shape of the cavity, which becomes elliptical during expansion, we calculated the eccentricity ($e$) of the cross-section, defined as $e = 100(M/m - 1)$ where $M$ and $m$ correspond to the major and minor axis of the cavity cross section, respectively. Figure 5 shows the differences in cross-section area and shape along the device axis for each cavity length, soil density and surcharge stress tested.

Results suggest that density has the highest influence on the area of the device, showing that larger cavity deformation and higher eccentricity occur in looser specimens. As expected, the cross sections towards the middle of cavity, furthest away from the circular clamps, exhibit the largest eccentricity. Similarly, results suggest that a lower vertical stress promotes eccentricity. Figure 6 shows the mean cross-sectional area for each test, and the ratio between the maximum and mean areas, as a measure of homogeneity along the device. Similarly, Figure 7 shows the mean eccentricity and the ratio between the maximum and mean eccentricity values along the cavity.

Results show that the area of the cross section of the cavity (orthogonal to the cavity axis) is multiplied by 1.7 to 2.5, with eccentricities between 6% and 19%. For most of the tests, increased soil density seems to restrict the expansion of the cavity, resulting in smaller and less eccentric (closer to circular) expansion of the cavities.

### Soil Strain field

In the following, we analyse the deformation of the soil mass due to the expansion of the cavity. Focusing mainly on the front (XZ plane - orthogonal to the cavity axis) and the side (YZ plane) views. From the displacement field obtained from the DVC (see image analysis section) the transformation gradient tensor (**F**) is obtained as shown in Eq 2.

$$\mathbf{F} = \frac{\partial \mathbf{x}}{\partial \mathbf{X}} = \mathbf{I} + \frac{\partial \mathbf{u}}{\partial \mathbf{X}} \qquad (2)$$

Where $\mathbf{X}$ and $\mathbf{x}$ are the position vectors in the reference and deformed configuration respectively, $\mathbf{I}$ is the identity tensor and $\mathbf{u}$ is the displacement vector calculated from DVC. The second-order tensor $\mathbf{F}$ is decomposed as $\mathbf{F} = \mathbf{R}.\mathbf{U}$, where $\mathbf{R}$ is an orthogonal (unitary) rotation tensor and $\mathbf{U}$ is the symmetric right-hand stretch tensor. In the following, soil strain is quantified by means of the magnitude ($|U|$) and isotropic and deviatoric parts of the right-hand stretch tensor, calculated as shown Eq. 3.

$$|U| = \mathbf{U}_{iso} : \mathbf{U}_{dev}$$
$$\mathbf{U}_{iso} = J^{1/3}\mathbf{I} \qquad (3)$$
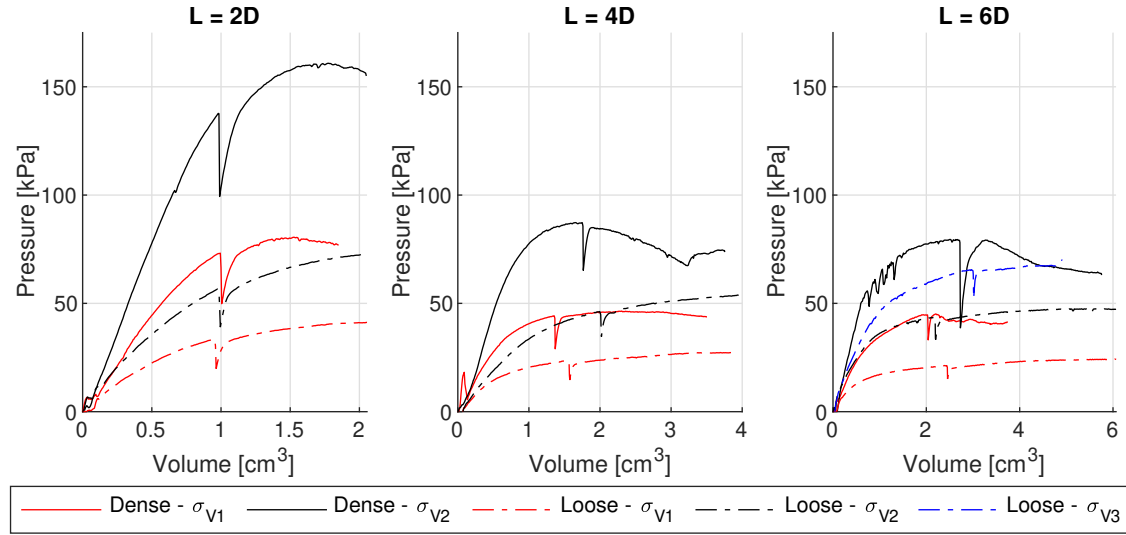$$\mathbf{U}_{dev} = J^{-1/3}\mathbf{U}$$

**Fig. 4.  Pressure vs. Volume response of the cavities. Dashed and solid lines correspond to experiments in loose and dense soil respectively. Different surcharge vertical stresses are shown in different line hues. Note that the pressure scale in the left-most plot is different to the other two, due to large differences in magnitude range.**
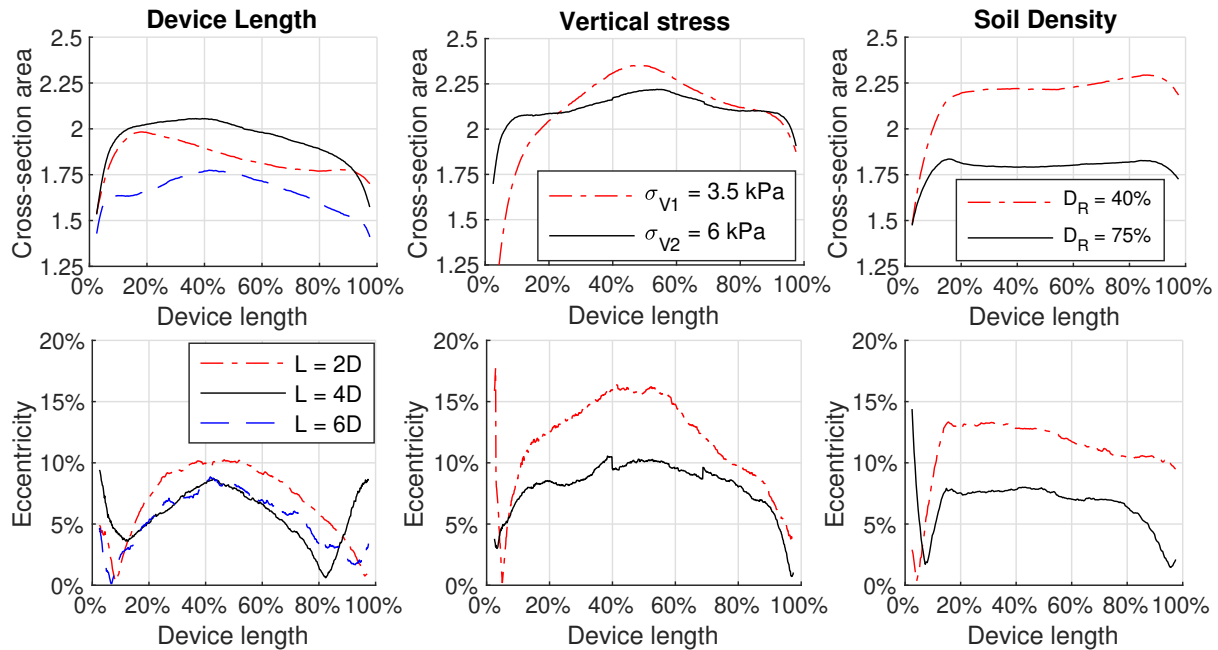


**Fig. 5.  Effect of device length, surcharge vertical stress and soil specimen density on the cross-sectional area and shape of the pressurised cavities. The cross sectional area is normalised by the initial cavity area. Eccentricity is calculated as the ratio between the major and minor axis of the cavity cross-section minus one. The left column (Device length specimens) shows results of experiments performed on loose specimens under a vertical stress $\sigma_{V2}$. The middle column (vertical stress specimens) corresponds to a device length of 6D in loose soil. The right column (Density specimens) shows results for devices with a length equal to 2D and a vertical stress of $\sigma_{V2}$.**

Where $J$ is the Jacobian (determinant of $\mathbf{U}$), and $\mathbf{U}_{iso}$ and $\mathbf{U}_{dev}$ are the isotropic and deviatoric parts of the right-hand stretch tensor respectively. The adopted scalar measurements of volumetric and deviatoric strains are $J - 1$ and $|\mathbf{U}_{dev}|$ respectively. In Figures 8-11, we use colormaps to show the components of strain generated in the soil; non-converging pixels (e.g. locations were the DVC algorithm failed to correlate the deformation) and the body of the expanding cavity are shown in black.

Regardless of the test variables, the strain fields exhibit two overlapping mechanisms: a zone of high strain around the cavity itself, reminiscent of cavity expansion; and a failure surface that extends from the bottom of the cavity to the free surface, typical of a passive trapdoor mechanism. An additional disturbance zone above the cavity, inside the region enclosed by the failure surface, is also observed in later stages of the expansion. Figure 8 exemplifies these mechanisms displaying the strain magnitude (2-norm of the stretch tensor $\mathbf{U}$).

**Deviatoric Strain**

The deviatoric strain scalar is calculated as the Euclidean norm of the deviatoric part of the stretch tensor ($\mathbf{U}$). Results in the loose specimens suggest that the pressurisation of shorter cavities (L = 2D), closer to a spherical shape, produces a concentric region of strain with less prevalent shear bands, contrary to longer cavities that yield shear bands. Conversely,
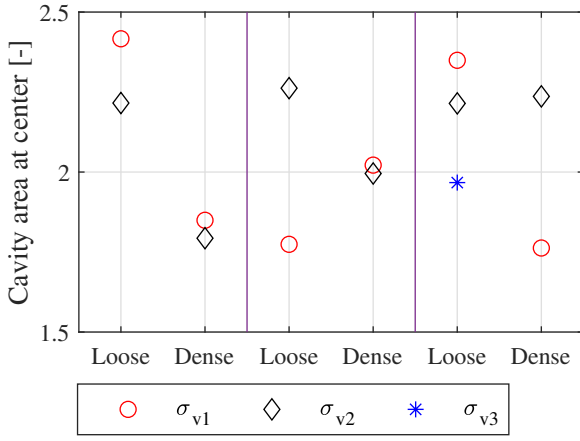
**Fig. 6.** Mean cross-sectional area in the middle of the cavity. The areas have been normalized by their initial cross-section area and shown for the different tests at full expansion.
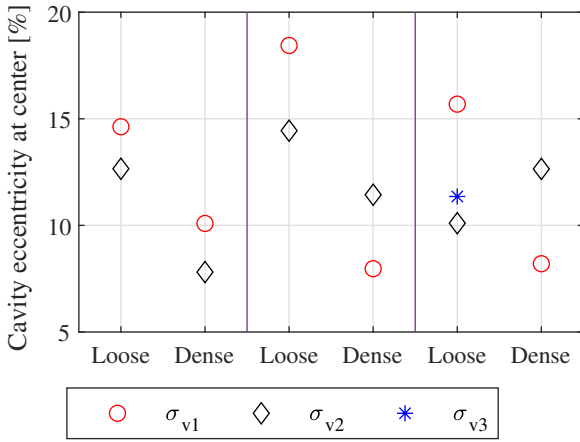


**Fig. 7.** Mean cross-sectional eccentricity in the middle of the cavity. Eccentricity is calculated as the difference between the length of the major and minor axes of the cavity and is shown as a percentage.

dense specimens exhibit a higher concentration of strain along the shear planes when compared to looser specimens, even in the shorter cavities. Figures 9 and 10 show the deviatoric strain fields in loose and dense specimens respectively.

**Volumetric Strain**

The volumetric strain is calculated as $J - 1$, where $J$ is the determinant of the stretch tensor, with dilation counted positive and contraction counted negative. In loose specimens, a zone of dilation generates around the cavity, and contraction is observed along the shear planes, even before they have fully developed. Conversely, in dense specimens, soil dilation is predominant both around the cavity and along the shear planes. It is also worth noting that the magnitude of the volumetric strain is significantly higher in the dense specimens than in the loose specimens. Figures 11 and 12 exemplify the distributions of volumetric strain in loose and dense specimens respectively.

**Porosity change**

Calculation of porosity change confirms that the material along the shear planes compacts in loose specimens and dilates in dense specimens. A dilation region around the pressurised cavity was present in every test, irrespective of the specimen

density, applied stress or cavity length. Fig 13 and Fig 14 show the change in porosity for loose and dense specimens, respectively.

DISCUSSION

*Characterisation of failure zone*

The failure zone includes a concentric region of strain around the cavity and curved shear planes that develop around the cavity and extend to the surface. In the following, we show that the shape that encloses the entire failure surface in the XZ plane (front view) follows that of a catenary. Then we focus on the shear bands that extend to the surface and quantify their orientation (using a straight line approximation), their thickness. We aslo measure the strain and porosity changes of the material inside the shear bands.

**Failure zone shape characterisation**

The shear zone generated during the expansion describes a bell shape, with its vertex below the invert of the cavity and convex branches extending to the surface (see Fig 8). In order to characterise such shape, we manually picked the boundary of the shear region from the front cross-section of the maximum shear strain (absolute difference between the major and minor principal strain increments) using a threshold of 7.5%, which allowed a clear distinction between the shear planes and the material around them, and consistency of the results across all the different tests. We found that the shear region describes a catenary shape, described by the equation:

$$z = a * \cosh\left(\frac{x - x_c}{a}\right) - z_c \tag{4}$$

where $x_c$ and $z_c$ correspond to centering coordinates in the $x$ and $z$ axis respectively, and $a$ is a shape parameter. Table 1 shows the obtained values for the shape parameter $a$. The coefficients of determination were $R^2 >= 0.9$.

| **Stress** | $\sigma_{V1}$ | | | $\sigma_{V2}$ | | | $\sigma_{V3}$ |
|---|---|---|---|---|---|---|---|
| **Length** | **2D** | **4D** | **6D** | **2D** | **4D** | **6D** | **6D** |
| **Loose** | 22.0 | 27.4 | 29.2 | 27.7 | 28.1 | 30.2 | 34.1 |
| **Dense** | 22.7 | 25.4 | 29.0 | 27.7 | 25.3 | 32.4 | - |

**Table 1.** Shape characterisation of the failure zone: values of the shape parameter of the catenary $a$ for the different experimental variables. Smaller values of $a$ correspond to curves with a higher curvature.

The shape of shear zones has been studied for similar loading scenarios, including uplift capacity of anchors, uplift resistance of buried pipes, and limit analysis of shallow tunnels. For instance, Zhao *et al.* (2018) studied the pullout of flat, circular anchors and described the shape of the failure surface as a "spatial funnel", with radially symmetric convex boundaries. Mallett *et al.* (2018) obtained similar results for the failure surface of root-like anchors using CT-scanning. Literature on the uplift resistance of buried pipes, in which circular inclusions are pulled vertically assuming plane strain conditions, have shown concave shapes starting between the waist and the crown of the pipes (Cheuk *et al.*, 2008). More recently, Zhang & Yang (2018) developed a limit analysis formulation for pressurised shallow tunnels, which resembles the loading conditions of
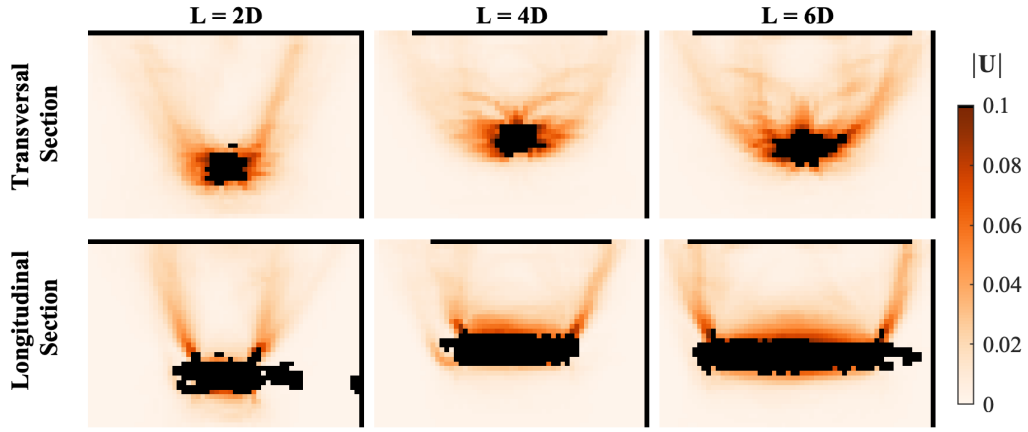
**Fig. 8. Strain magnitude calculated as the Euclidean norm of the stretch tensor (U). Values shown for tests in "dense" specimens and vertical surcharge $\sigma_{V1}$.**
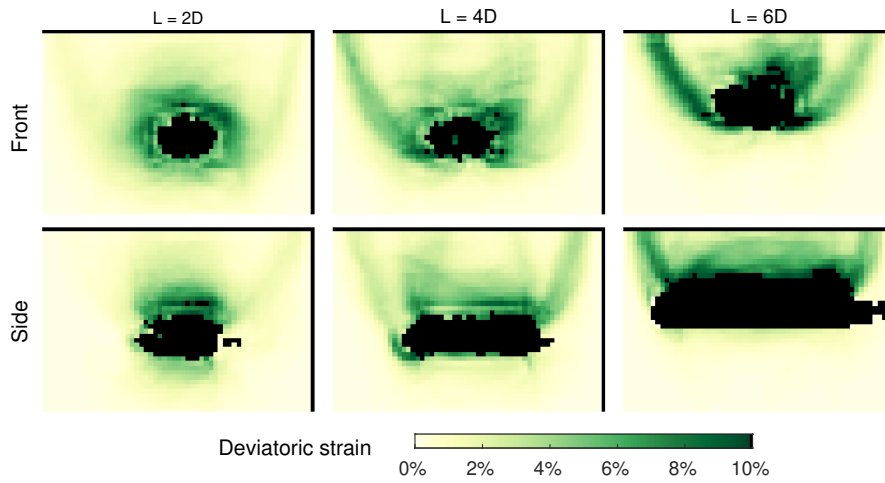


**Fig. 9. Euclidean norm of the deviatoric part of the stretch tensor in loose specimens. Shown fields correspond to the tests with a vertical surcharge $\sigma_{V1}$.**
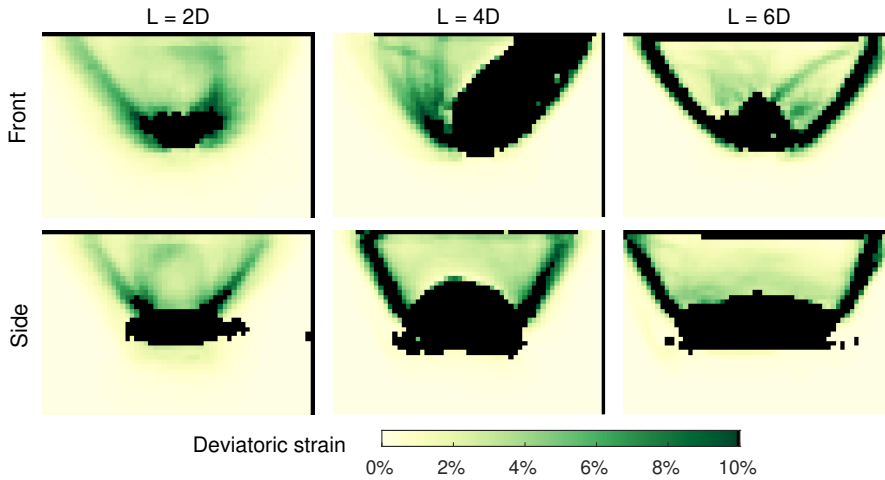


**Fig. 10. Euclidean norm of the deviatoric part of the stretch tensor in dense specimens. Shown fields correspond to the tests with a vertical surcharge $\sigma_{V1}$.**

the present study, but still shows failure planes that do not completely enclose the cavity.

Contrary to the results reported in the literature (Cheuk *et al.*, 2008; Zhang & Yang, 2018), our experimental results show that the shear region is convex and completely encloses the cavity. The results from Table 1 suggest that higher vertical stress results in less concave failure zones (which tend to be more straight lines). Shorter cavities in loose soil exhibit a more ductile response, with no evidence of peak resistance or shear bands and result in highly curved failure zones, which
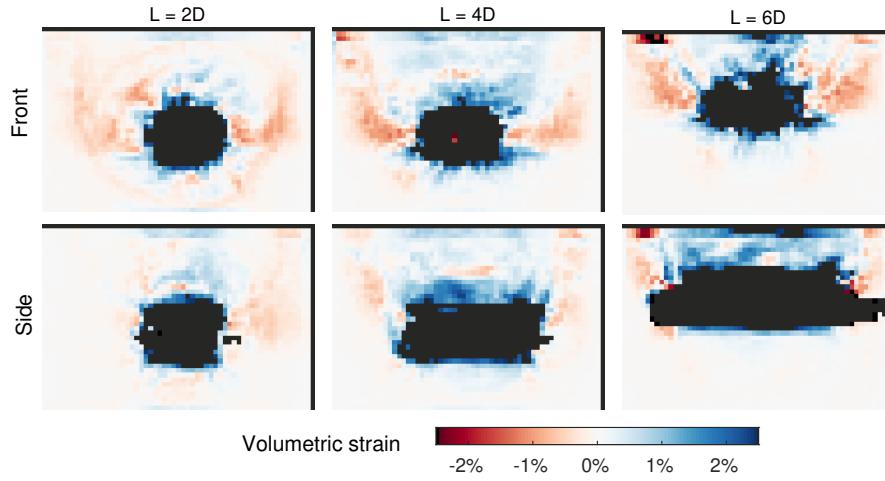
**Fig. 11.** Volumetric strain in loose specimens. The volumetric strain is calculated as $J - 1$, where $J$ is the determinant of the stretch tensor. Negative and positive strains correspond to contraction and dilation, respectively. Shown fields correspond to the tests with a vertical surcharge $\sigma_{V1}$.
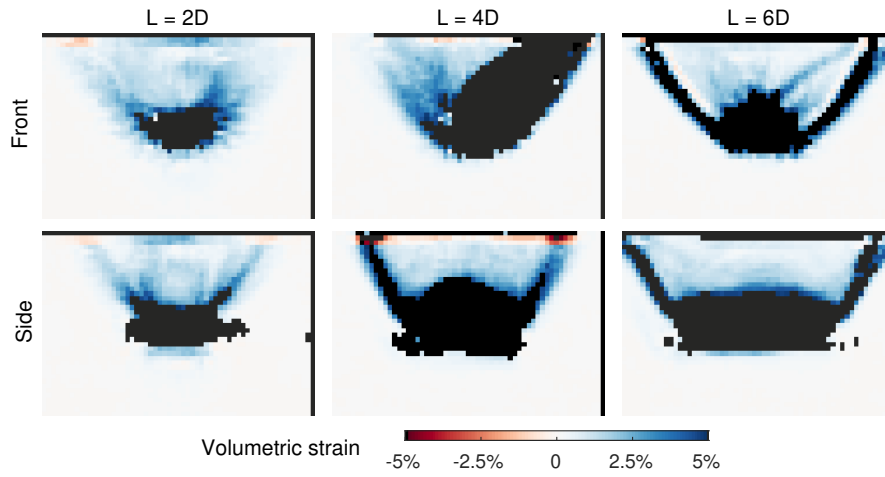


**Fig. 12.** Volumetric strain in dense specimens. The volumetric strain is calculated as $J - 1$, where $J$ is the determinant of the stretch tensor. Negative and positive strains correspond to contraction and dilation, respectively. Shown fields correspond to the tests with a vertical surcharge $\sigma_{V1}$.
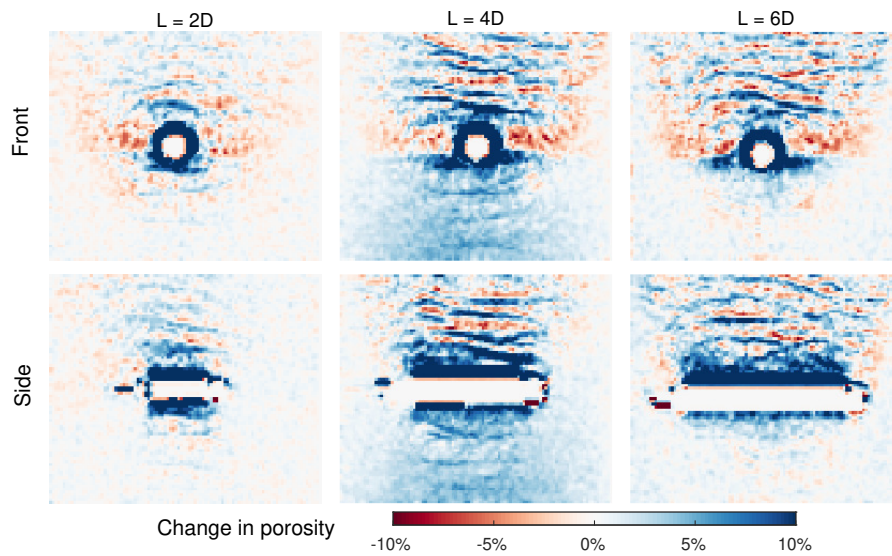


**Fig. 13.** Change in porosity in loose specimens, calculated as the absolute porosity change between the final expansion step and the initial state. A negative change in porosity corresponds to densification and a positive change, to loosening. Shown fields correspond to the tests with a vertical surcharge $\sigma_{V1}$.
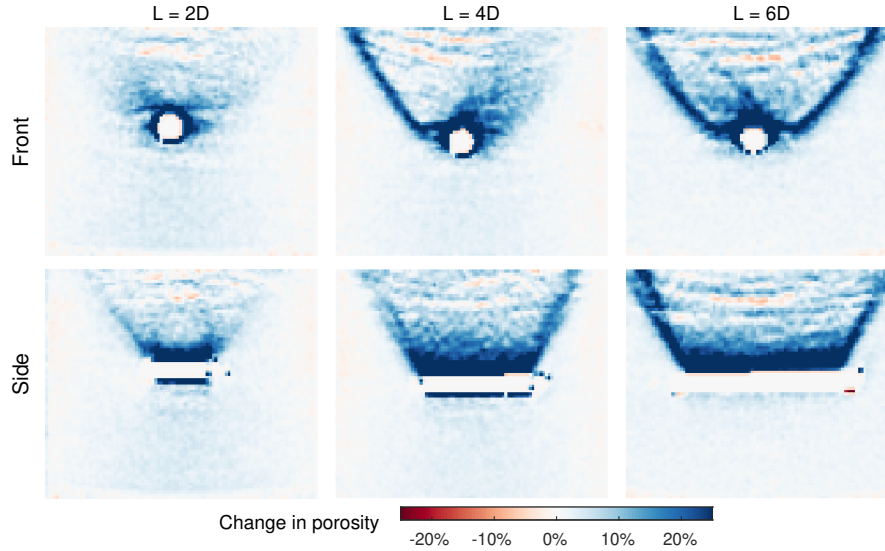
**Fig. 14. Change in porosity in dense specimens, calculated as the absolute porosity change between the final expansion step and the initial state. A negative change in porosity corresponds to densification and a positive change, to loosening. Shown fields correspond to the tests with a vertical surcharge $\sigma_{V1}$.**

agrees with the observations by Cheuk *et al.* (2008). The stark difference of failure mechanism between short (L=2D) and longer cavities (L=4D and L=6D) coincides with the difference in the pressure-volume response (Fig 4).

**Average orientation and thickness of shear bands (front view)**

After characterising the failure zone as a catenary-shaped band, we measured the average orientation and thickness of the shear bands that reach the free surface. For each test, we identified shear bands manually (like for the entire failure zone) and computed the medial axis of each shear band. The medial axis, also known as skeleton, is a common feature used in image processing, and corresponds to the set of points inside the region which are equidistant to more than one edge of the region. The distance from the medial axis of the shear band to its boundaries corresponds to half the shear band width. This distance, initially calculated in pixels, was transformed into millimeters and compared to the mean grain size of the soil ($d_{50} = 0.34mm$), the accuracy of these measurements is limited by the size of the pixels in the strain map obtained from the DVC, where one pixel corresponds to 6.4 times $d_{50}$ or about 2.2mm.

Results, provided in Table 2, show that the thickness of the shear bands is between 8.1 and 20.6 $\pm 6.4$ times the mean grain diameter, without clear influence of the tested variables (soil density, surcharge stress and probe length) in the values. These findings agree with with other experimental results reported in the literature, in which the shear band thickness is between 5 and 20 times the mean grain size regardless of test variables (Mühlhaus & Vardoulakis, 1987; Vermeer, 1990; Desrues & Viggiani, 2004).

Next, the orientation angle of the shear bands was calculated. Since the shear bands were curved, specially in the neighborhood of the cavity, we used the two thirds of the medial axis closest to the free surface to calculate the orientation angle of the shear bands. That portion of the medial axis was then fitted using a linear regression and the slope was transformed into an angle measured from the vertical (Z direction). Obtained results are shown in Table 3.

Note that the missing values in Table 2 and Table 3 correspond to the tests with the shortest cavity (L = 2D) in

| Stress | $\sigma_{V1}$ | | | $\sigma_{V2}$ | | | $\sigma_{V3}$ |
|---|---|---|---|---|---|---|---|
| **Length** | **2D** | **4D** | **6D** | **2D** | **4D** | **6D** | **6D** |
| **Loose** | - | 12.8 | 18.1 | - | 17.6 | 18.1 | 16.2 |
| **Dense** | 8.1 | 20.6 | 13.8 | 11.4 | - | 17.1 | - |

**Table 2. Shear Band thickness (width), measured relative to the mean grain size diameter ($d_{50}$).**

| Stress | $\sigma_{V1}$ | | | $\sigma_{V2}$ | | | $\sigma_{V3}$ |
|---|---|---|---|---|---|---|---|
| **Length** | **2D** | **4D** | **6D** | **2D** | **4D** | **6D** | **6D** |
| **Loose** | - | 24.8 | 28.5 | - | 26.8 | 34.4 | 40.9 |
| **Dense** | 31.1 | 29.9 | 38.2 | 39.5 | - | 38.9 | - |

**Table 3. Shear band orientation. Values in degrees measured from the vertical. Angles were obtained from the linear fit of the medial axis of the shear band, discarding the highly curved section adjacent to the cavity.**

loose soil, which did not exhibit well defined shear bands, while the test with variables (L = 4D, $\sigma_{V2}$ and dense soil) showed significant distortion and therefore it was not possible to identify the shear bands.

According to previous studies on the uplift resistance of buried pipes (White *et al.*, 2001; Cheuk *et al.*, 2008; White *et al.*, 2008), the inclination angle of the shear bands (measured from the vertical) is correlated to the dilation angle ($\psi$) of the material; the maximum dilation angle for Hostun sand was reported to be between 11 and 14 degrees (Schanz & Vermeer, 1996), although its actual value depends on the stress state and density of the soil mass. Results reported in Table 3 are in agreement, showing that higher vertical surcharge stress and increased soil density, expected to trigger stronger dilatant behavior, result in higher angles of orientation of the shear bands.

**Strain and porosity change inside the shear bands**

We calculated the volumetric strain and the change in porosity inside the shear bands. Average values are reported in Table 4.

| Stress | | $\sigma_{V1}$ | | | $\sigma_{V2}$ | | | $\sigma_{V3}$ |
|---|---|---|---|---|---|---|---|---|
| Length | | 2D | 4D | 6D | 2D | 4D | 6D | 6D |
| Loose | V | - | -0.07 | 0.52 | - | -0.51 | 0.02 | 0.77 |
| | P | - | -0.33 | -1.63 | - | -1.11 | 0.92 | 0.28 |
| Dense | V | 3.47 | 3.41 | 3.22 | 2.25 | - | 5.36 | - |
| | P | 8.79 | 9.61 | 7.68 | 5.43 | - | 14.75 | - |

**Table 4. Volumetric strain and change of porosity inside shear bands. V - Mean volumetric strain inside the shear bands [%] P - Mean porosity change inside shear bands. [%]**

Results from Table 4 show a linear relationship ($R^2 = 0.96$) between the change in porosity (and therefore change in void ratio) and the volumetric strain generated by the expansion of the cavity inside the shear bands. Additionally, it can be observed that the changes inside the shear bands in loose specimens are smaller in magnitude compared to dense specimens. The soil along the shear bands in loose state slightly dilates or contracts, while it significantly dilates when initially in dense state.

Table 5 shows the final void ratio achieved in the shear bands. Results show that the terminal void ratio (e) inside the shear bands reaches values above the value ($e = 1$) reported for the minimum density (Desrues & Viggiani, 2004; Andò, 2013), which is in agreement with the findings of Oda & Kazama (1998), who showed that the density of the material along the shear bands can reach values below the minimum used to calculate relative density. Similarly, Alshibli & Hasan (2008) found increments of up to 24.7% in the void ratio inside shear bands in triaxial tests, while we found average increments of 22.5% 68.8% in loose and dense specimens respectively.

| Stress | $\sigma_{V1}$ | | | $\sigma_{V2}$ | | | $\sigma_{V3}$ |
|---|---|---|---|---|---|---|---|
| Length | 2D | 4D | 6D | 2D | 4D | 6D | 6D |
| Loose | - | 1.19 | 1.20 | - | 1.10 | 1.03 | 1.06 |
| Dense | 0.89 | 1.52 | 1.18 | 1.31 | - | 1.68 | - |

**Table 5. Final void ratio inside shear bands [-]. Average values inside identified regions corresponding to shear bands in the different tests. Initial void ratios (e) for the loose and dense specimens were $0.91$ and $0.78$ respectively.**

Fig 15 shows the change of the void ratio along the shear bands over the different expansion steps. Several authors have proposed that the void ratio inside shear bands converges to a critical value (Roscoe, 1970; Desrues et al., 1996) and Evans & Frost (2010); Narsilio & Santamarina (2008) further proposed that such value depends on the initial void ratio of the soil. Results from Fig 15 further demonstrates the different behavior between loose and dense specimens: loose specimens exhibit signs of convergence, while dense specimens did not. In addition, void ratios inside shear bands are significantly higher in dense specimens compared to loose ones and are inversely proportional to the vertical surcharge stress in our experiments.

*Orientation of principal strain increments*

Principal strain increments and their respective orientations are obtained from the eigen-decomposition of the right-hand stretch tensor (**U**) as shown in Eq 5.

$$\mathbf{U} = \sum_{i=1}^{3} \lambda_i (\mathbf{r_i} \otimes \mathbf{r_i}) \qquad (5)$$

Where the $\lambda_i$ correspond to the principal strain increments (eigenvalues) and the $\mathbf{r_i}$ correspond to the orientation of the principal strain increments (eigenvectors).

The obtained vector fields following the orientation of strain increments were similar for tests with different densities and vertical surcharge levels, but showed differences as a function of the length of the cavity. Figure 16 exemplifies such differences, showing the orientation of the strain increments for two tests with different densities, surcharge stresses and cavity lengths. The lines in Figure 16 correspond to streamlines in the vector field, and therefore show the direction of the strain increments only, regardless of their magnitude.

From the front view, we observe that the minor strain increment is horizontal on both sides of the expanding cavity, while it is vertical at the top and bottom of the cavity. Conversely, the major strain increment is parallel to the cavity at the crown, bottom and sides of the cavity. In between, the major strain increment is oriented at an angle, forming an "X" shape. It is worth noting that the shear bands are oriented in the direction of the major strain increment, while the minor strain increment is normal to it.

From the side view, we note that the orientation of the strain increments around the shorter cavity (L = 2D) is similar to that in the front view, suggesting that the failure mechanism is close to that of a spherical pressurised cavity. By contrast, the longer cavity ($L = 6D$) still exhibits the "X" shape of the major strain increment (oriented along the shear bands), but with an intermediate region in which both the major and minor strain increments are normal to the body of the cavity. From the top view, we note that the major principal strain increment is oriented normal to the body of the cavity. In the middle of the cavity axis, the major and minor strain increments are normal to the cavity and parallel to each other, suggesting the existence of plane strain conditions localized around the center of the cavity. We explore this observation in detail in the following section.

Previous studies have proposed that the stress and strain fields around the cavity are non-coaxial during early steps of plastic expansion due to the reorientation of principal stresses around the cavity (Miura et al., 1986; Yang & Yu, 2010; Chen & Huang, 2020). After the soil has reached its yield point, it was shown that stress and strain become coaxial (Ishihara & Towhata, 1983; Cai et al., 2013). Hence, we hypothesize that the orientations of strain increments shown here correspond to the orientation of the principal stresses inside the soil as well, since they show a state after the yield point of the material, after significant deformation has accumulated.

Previous studies on the orientation of principal stresses during arching date back to the work of Handy (1985), who studied arching (active trapdoor) in vertical trenches or silos and proposed the orientation of the minor principal stresses forms an arch that follows a catenary shape, as described by Eq 4. Such observations were validated by Harrop-Williams (1989) who showed the shape resembles a catenary or a circle. More recently, Chevalier et al. (2012) found that the shape of the catenary arch formed above the trapdoor follows the orientation of the major principal stresses and that the peak friction angle influences the extent of such arch. Furthermore, Guo & Zhou (2013) found that an arch develops along the orientations of the
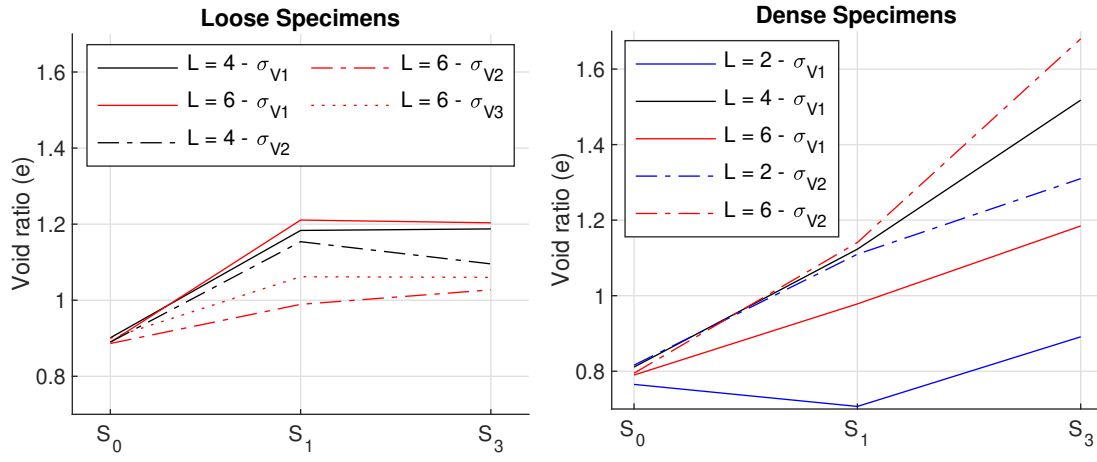
**Fig. 15.  Change in void ratio inside shear bands over the expansion steps. Average void ratio along the location of the shear bands before expansion ($S_0$), and for the subsequent expansion steps $S_1$ and $S_2$.**
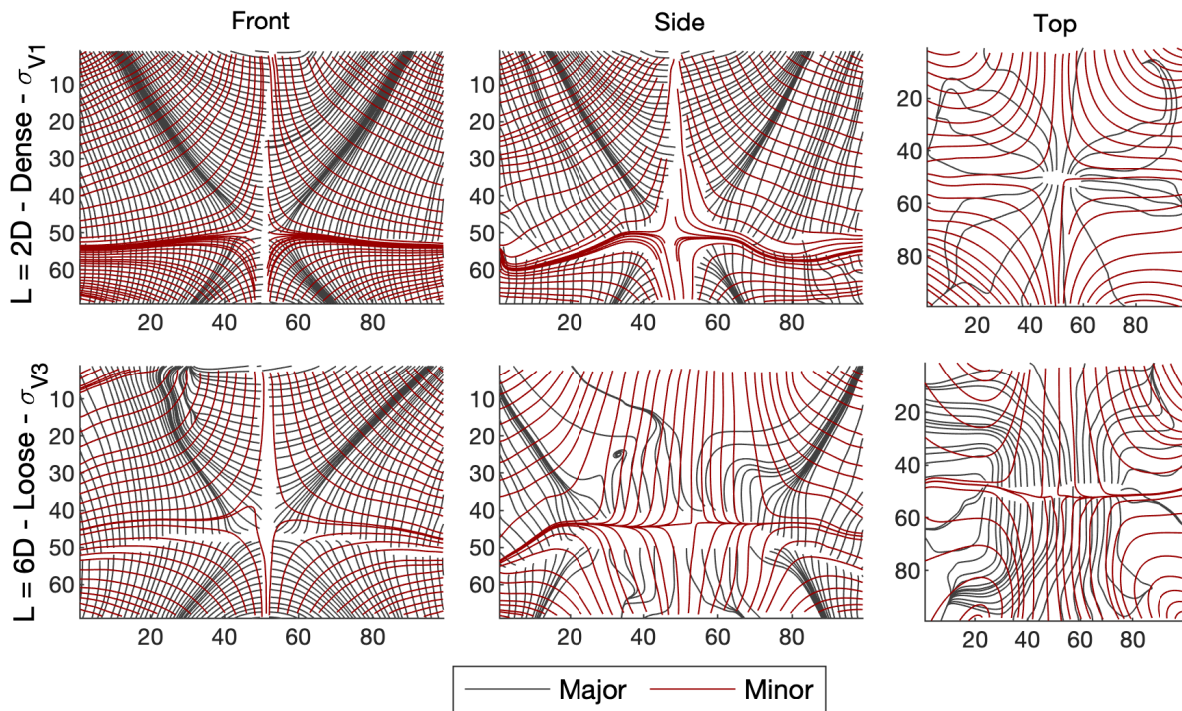


**Fig. 16.  Orientation of principal strain increments. Lines correspond to streamlines following the orientation of the major and minor principal strain increments. Shown orientations correspond to the projection of the corresponding eigenvectors onto each view (front, side, top).**

principal stresses to form a stress free surface that is adequately characterised by a parabola or a truncated ellipse in soils with higher friction angles.

Dalvi & Pise (2012) expanded the findings from Handy (1985) to the passive arching case, more relevant to our study, and found that the alignment of the principal stresses during this loading mechanism also follows the shape a catenary. Moreover, Wong & Kaiser (1991) studied the collapse mechanisms of shallow tunnels in cohesionless soil, and proposed that the catenary-shaped orientation of stresses appears both as downward oriented catenaries during cavity roof collapse, or as upward oriented catenaries that reach the free surface during the complete failure of the cavity, as shown in the failure mechanism exemplified in Fig 8 and Fig 16.

*Plane Strain validation*

The vast majority of analytical solutions proposed for cavity expansion problems assume plane strain conditions. We evaluate the validity of this assumption in our experiments, in which the length of the cavity was equal to two to six times the diameter. Minor and major principal strain increments are orthogonal to each other in the YZ and XY views, which is an indicator of plane strain conditions in the XZ plane (cross-section of the cavity). To quantify the deviation from plane strain conditions in the XZ plane, we define the plane strain deviation index ($PSD$) as follows:

$$PSD = 1 - \frac{\|\mathbf{U}_{2D}\|}{\|\mathbf{U}_{3D}\|} \qquad (6)$$

where $\|\mathbf{U}_{2D}\|$ is the magnitude of the 2D stretch tensor ignoring the out-of-XZ-plane components, and $\|\mathbf{U}_{3D}\|$ is the

magnitude of the 3D stretch tensor. The PSD index, shown as a percentage, ranges from 0% for perfect plane strain conditions, to 100% for the worst case scenario, in which all the strain occurs in the out-of-plane direction. Figure 17 shows the map of plane strain loss for each of the tested cavity lengths, indicating that plane strain conditions are restricted to a region around the center of the cavity, and as expected, the extent of such region is proportional to the total length of the cavity.

Furthermore, we calculated the weighted average of the PSD along the cross sections ($\overline{PSD}$) of the cavity (parallel to the XZ plane), as follows:

$$\overline{PSD} = \frac{\sum(PSD \cdot \|\mathbf{U_{3D}}\|)}{\sum \|\mathbf{U_{3D}}\|} \quad (7)$$

Figure 18 shows the average deviation from plane strain conditions along the axis of the cavity, for the 13 different tests, after the second inflation step. Results show that even though the deviation at the edges of the cavity is similar for all the different lengths, the region of low deviation from plane strain is larger for more slender (longer) cavities.

In order to better understand the influence of cavity length, soil density and vertical load on the extent of the region under plane strain conditions, we also calculated the percentage of the cavity length that has an average PSD below 5%. We compared that percentage for the different test variables (Fig 19), and we followed the evolution of that length with the inflation steps (Fig 20).

As expected, longer cavities are closer to plane strain conditions. Yet, at least 25% of the length of the longest devices (L = 6D) did not meet plane strain conditions (Figures 18 and 19). Results suggest that the higher soil density and the higher surcharge vertical stress, the more likely plane strain conditions. This observation confirms previous results on cavity deformation (Figure 7): a more cylindrical shape is more likely to occur at higher stress and in denser soils. Overall, pressurisation promotes plane strain conditions, especially in dense soil (Figure 20).

## CONCLUSIONS

Pressurisation of a small-scale cylindrical cavity embedded in sand under geostatic stress caused a failure mechanism characterised by a concentric plastic deformation zone, typical of cavity expansion, combined with catenary-shaped shear bands typical of anchoring. The failure mechanism around shorter cavities (with length equal to twice the diameter) was closer to a paraboloid (symmetric radially) while longer cavities exhibit a plane strain region along their axis. From x-ray computed tomography images, it was noted that the soil adjacent to the cavity dilated regardless of the initial density of the soil, but inside shear bands, it either dilated in dense specimens or slightly contracted in loose specimens. The curvature of the failure planes was more concave in loose soil under low vertical stress. As density and vertical stress increased, the failure zones became closer to planes. The orientation at which the shear bands reach the surface was proportional to the dilation angle of the soil, which is a function of soil density and stress state as shown in the results.

The orientation of the principal strain increments, assumed to be coaxial with stress at large deformation stages, also aligned with a catenary shape along the longitudinal cross section of the cavity. Our study shows that the plane strain assumption currently made in state-of-the-art analytical models of cavity expansion does not hold for short cavities or tunnels at shallow depth (hence under biaxial stress) and even in the longest of the cavities tested (with a length six times larger than the diameter), plane strain conditions were only met over 75% of the cavity length. Additionally, shear strain was not negligible around the cavity, contrary to common modeling assumptions.

These results are important to the fundamental understanding of failure mechanisms at shallow depth, the prediction of failure modes and transitions of failure modes, and the design of subsurface geotechnical structures in sand, relevant to Horizontal Directional drilling (HDD), pipe uplift, micro-tunneling, and resource exploitation.

## REFERENCES
Alshibli, K. A. & Hasan, A. (2008). Spatial variation of void ratio and shear band thickness in sand using X-ray computed tomography. *Géotechnique* **58**, No. 4, 249–257, doi:10.1680/geot.2008.58.4.249, URL http://www.icevirtuallibrary.com/doi/10.1680/geot.2008.58.4.249.

Andò, E. (2013). *Experimental investigation of microstructural changes in deforming granular media using x-ray tomography*. Ph.D. thesis, Université de Grenoble.

ASTM (2011). F1962-11 standard guide for use of maxi-horizontal directional drilling for placement of polyethylene pipe or conduit under obstacles, including river crossings **04**, 1–18, doi:10.1520/F1962-11.1.

Atkinson, J. H. & Potts, D. M. (1977). Stability of a shallow circular tunnel in cohesionless soil. *Géotechnique* **27**, No. 2, 203–215, doi:10.1680/geot.1977.27.2.203, URL http://www.icevirtuallibrary.com/doi/10.1680/geot.1977.27.2.203.

Bennett, D. & Ariaratnam, S. T. (2017). *Horizontal directional drilling: Good practices guidelines*. 4th edn., North American Society for Trenchless Technology.

Biarez, J. & Hicher, P. Y. (1994). Elementary mechanics of soil behaviour: saturated remoulded soils. In *Elementary mechanics of soil behaviour: saturated remoulded soils.*, Rotterdam: A.A. Balkema.

Cai, Y., Yu, H.-S., Wanatowski, D. & Li, X. (2013). Noncoaxial Behavior of Sand under Various Stress Paths. *Journal of Geotechnical and Geoenvironmental Engineering* **139**, No. 8, 1381–1395, doi:10.1061/(ASCE)GT.1943-5606.0000854.

Caicedo, B. (2018). *Geotechnics of Roads: Fundamentals*. London: CRC Press, doi:10.1201/9780429025914, URL https://www.taylorfrancis.com/https://www.taylorfrancis.com/books/mono/10.1201/9780429025914/geotechnics-roads-fundamentals-bernardo-caicedo.

Chapman, D., Metje, N. & Stark, A. (2018). *Introduction to tunnel construction*. 2nd editio edn., CRC Press.

Chen, Z. & Huang, M. (2020). Non-coaxial behavior modeling of sands subjected to principal stress rotation. *Acta Geotechnica* **15**, No. 3, 655–669, doi:10.1007/s11440-018-0760-4.

Cheuk, C. Y., White, D. J. & Bolton, M. D. (2008). Uplift Mechanisms of Pipes Buried in Sand. *Journal of Geotechnical and Geoenvironmental Engineering* **134**, No. 2, 154–163, doi:10.1061/(ASCE)
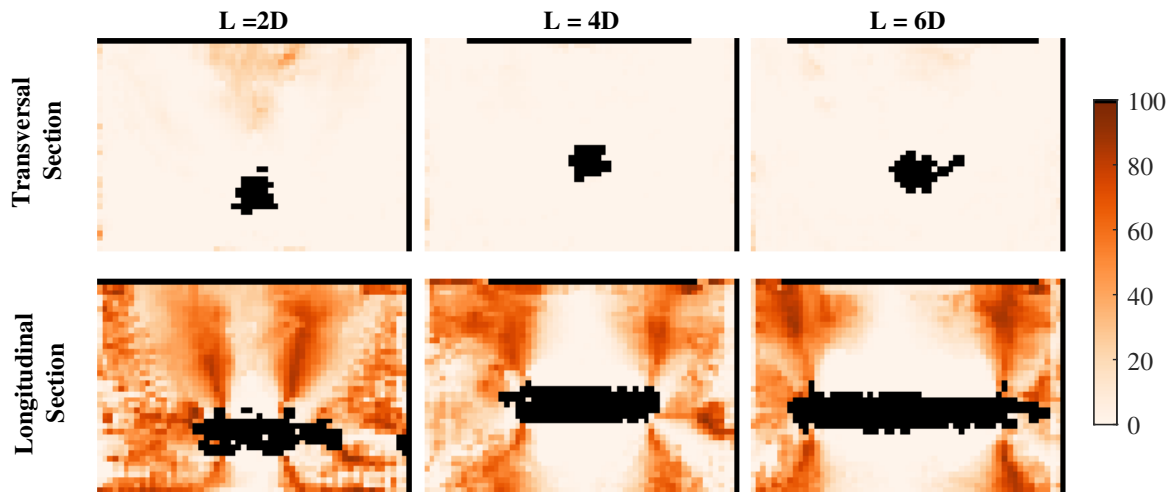
**Fig. 17.** Plane strain deviation (PSD) fields. The PSD index is calculated as the proportion of strain magnitude that is lost at a given location when plane strain conditions are assumed. A value of 0 corresponds to perfect plane strain (in the XZ plane) and a maximum value of 100 corresponds to a strain field oriented completely out of the XZ plane. Shown tests correspond to dense specimens with a vertical surcharge $\sigma_{V1}$.
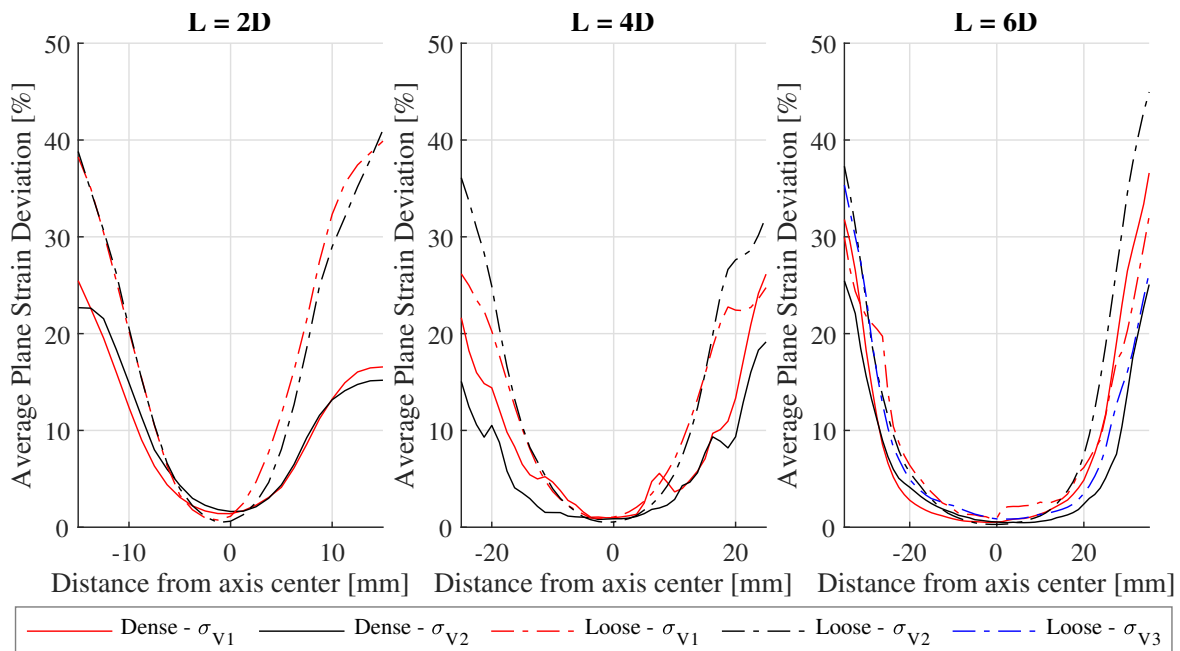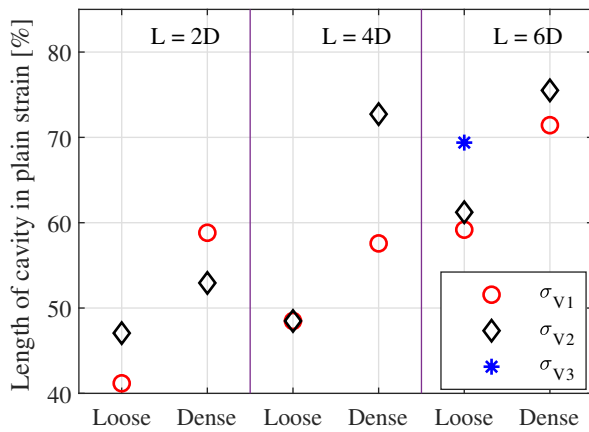


**Fig. 18.** Average plane strain deviation ($\overline{PSD}$). Values are calculated as the weighted average of the PSD index along cross sections normal to the cavity axis (parallel to the XZ plane). Values are weighted by the total strain magnitude.

1090-0241(2008)134:2(154), URL https://doi.org/10.1061/(ASCE)1090-0241(2008)134:2(154).

Chevalier, B., Combe, G. & Villard, P. (2012). Experimental and discrete element modeling studies of the trapdoor problem: Influence of the macro-mechanical frictional parameters. *Acta Geotechnica* **7**, No. 1, 15–39, doi:10.1007/s11440-011-0152-5.

Costa, Y. D., Zornberg, J. G., Bueno, B. S. & Costa, C. L. (2009). Failure Mechanisms in Sand over a Deep Active Trapdoor. *Journal of Geotechnical and Geoenvironmental Engineering* **135**, No. 11, 1741–1753, doi:10.1061/(ASCE)GT.1943-5606.0000134, URL http://ascelibrary.org/doi/10.1061/{%}28ASCE{%}29GT.1943-5606.0000134.

Dalvi, R. S. & Pise, P. J. (2012). Analysis of Arching in Soil-Passive State. *Indian Geotechnical Journal* **42**, No. 2, 106–112, doi:10.1007/s40098-012-0004-8, URL http://link.springer.com/10.1007/s40098-012-0004-8.

Desrues, J., Chambon, R., Mokni, M. & Mazerolle, F. (1996). Void ratio evolution inside shear bands in triaxial sand specimens studied by computed tomography. *Géotechnique* **46**, No. 3, 529–546, doi:10.1680/geot.1996.46.3.529, URL http://www.icevirtuallibrary.com/doi/10.1680/geot.1996.46.3.529.

Desrues, J. & Viggiani, G. (2004). Strain localization in sand: an overview of the experimental results obtained in Grenoble using stereophotogrammetry. *International Journal for Numerical and Analytical Methods in Geomechanics* **28**, No. 4, 279–321, doi:10.1002/nag.338, URL http://doi.wiley.com/10.1002/nag.338.

Evans, C. H. (1984). *An examination of arching in granular soils*. Ph.D. thesis, Massachusetts Institute of Technology, URL http://hdl.handle.net/1721.1/45181.

Evans, T. M. & Frost, J. D. (2010). Multiscale investigation of shear bands in sand: Physical and numerical experiments. *International*

**Fig. 19. Percentage of cavity length under plane strain conditions (PS). Results from the second inflation step. The criteria adopted to set PS corresponds to the cross sections with an average plane strain deviation (PSD) under 5%.**
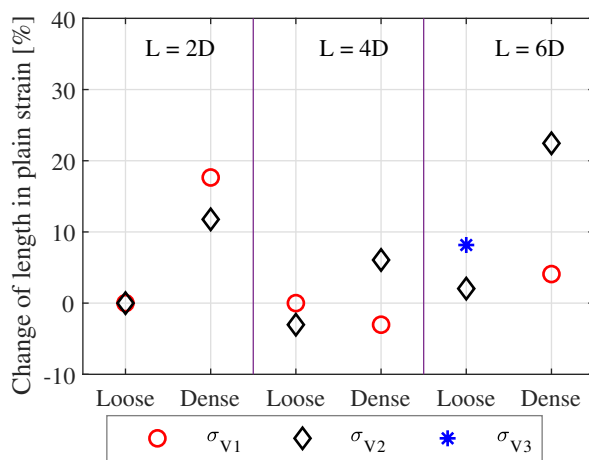


**Fig. 20. Change of cavity length under plane strain conditions (PS) between the last and first inflation steps.**

*Journal for Numerical and Analytical Methods in Geomechanics* **34**, No. 15, n/a–n/a, doi:10.1002/nag.877, URL http://doi.wiley.com/10.1002/nag.877.

Garnier, J., Gaudin, C., Springman, S., Culligan, P., Goodings, D., Konig, D., Kutter, B., Phillips, R., Randolph, M. & Thorel, L. (2007). Catalogue of scaling laws and similitude questions in geotechnical centrifuge modelling. *International Journal of Physical Modelling in Geotechnics* **7**, No. 3, 01–23, doi:10.1680/ijpmg.2007.070301, URL http://www.icevirtuallibrary.com/doi/10.1680/ijpmg.2007.070301.

Guo, P. & Zhou, S. (2013). Arch in granular materials as a free surface problem. *International Journal for Numerical and Analytical Methods in Geomechanics* **37**, No. 9, 1048–1065, doi:10.1002/nag.1137, URL http://doi.wiley.com/10.1002/nag.1137.

Handy, R. L. (1985). The Arch in Soil Arching. *Journal of Geotechnical Engineering* **111**, No. 3, 302–318, doi:10.1061/(ASCE)0733-9410(1985)111:3(302), URL https://doi.org/10.1061/(ASCE)0733-9410(1985)111:3(302).

Harrop-Williams, K. (1989). Arch in Soil Arching. *Journal of Geotechnical Engineering* **115**, No. 3, 415–419, doi:10.1061/(ASCE)0733-9410(1989)115:3(415), URL https://doi.org/10.1061/(ASCE)0733-9410(1989)115:3(415).

Hill, R. (1950). *The Mathematical theory of plasticity*. New York, New York, USA: Oxford University Press, doi:10.1038/252139a0.

Ishihara, K. & Towhata, I. (1983). Sand Response to Cyclic Rotation of Principal Stress Directions as Induced by Wave Loads. *Soils and Foundations* **23**, No. 4, 11–26, doi:10.3208/sandf1972.23.4_11.

Ji, X., Ni, P., Barla, M., Zhao, W. & Mei, G. (2018). Earth pressure on shield excavation face for pipe jacking considering arching effect. *Tunnelling and Underground Space Technology* **72**, 17–27, doi:10.1016/j.tust.2017.11.010.

Kennedy, M. J., Skinner, G. D. & Moore, I. D. (2006). Limiting Slurry Pressures to Control Hydraulic Fracturing in Directional Drilling Operations in Purely Cohesive Soil. *Transportation Research Record: Journal of the Transportation Research Board* **1976**, No. 1, 172–180, doi:10.1177/0361198106197600119, URL http://journals.sagepub.com/doi/10.1177/0361198106197600119.

Keulen, B. (2001). *Maximum allowable pressures during horizontal directional drillings focused on sands*. Ph.D. thesis, TU Delft, URL https://repository.tudelft.nl/islandora/object/uuid:ad91dad8-b958-481b-82d8-c7395d1a3874.

Lan, H. & Moore, I. D. (2017). Numerical Investigation of the Circumferential Stresses around Boreholes during Horizontal Directional Drilling. *International Journal of Geomechanics* **17**, No. 12, 04017114, doi:10.1061/(asce)gm.1943-5622.0001011, URL https://ascelibrary.org/doi/abs/10.1061/%28ASCE%29GM.1943-5622.0001011.

Lan, H. & Moore, I. D. (2018). Practical criteria for assessment of horizontal borehole instability in saturated clay. *Tunnelling and Underground Space Technology* **75**, 21–35, doi:10.1016/j.tust.2018.02.002.

Lan, H. & Moore, I. D. (2020). Experimental Investigation Examining Influence of Burial Depth on Stability of Horizontal Boreholes in Sand. *Journal of Geotechnical and Geoenvironmental Engineering* **146**, No. 5, 04020013, doi:10.1061/(ASCE)GT.1943-5606.0002222, URL https://ascelibrary.org/doi/abs/10.1061/%28ASCE%29GT.1943-5606.0002222http://ascelibrary.org/doi/10.1061/%28ASCE%29GT.1943-5606.0002222.

Lee, C. J., Wu, B. R., Chen, H. T. & Chiang, K. H. (2006). Tunnel stability and arching effects during tunneling in soft clayey soil. *Tunnelling and Underground Space Technology* **21**, No. 2, 119–132, doi:10.1016/j.tust.2005.06.003.

Li, L., Li, J. & Sun, D. (2016). Anisotropically elasto-plastic solution to undrained cylindrical cavity expansion in K0-consolidated clay. *Computers and Geotechnics* **73**, 83–90, doi:10.1016/j.compgeo.2015.11.022, URL http://dx.doi.org/10.1016/j.compgeo.2015.11.022.

Mair, R. J. & Wood, D. M. (1987). *Pressuremeter Testing : Methods and Interpretation*. 1st editio edn., Elsevier Science, doi:10.1139/t88-074.

Mallett, S. D., Matsumura, S. & David Frost, J. (2018). Additive manufacturing and computed tomography of bio-inspired anchorage systems. *Geotechnique Letters* **8**, No. 3, 219–225, doi:10.1680/jgele.18.00090.

Miura, K., Miura, S. & Toki, S. (1986). Deformation Behavior of Anisotropic Dense Sand Under Principal Stress Axes Rotation. *Soils and Foundations* **26**, No. 1, 36–52, doi:10.3208/sandf1972.26.36.

Mühlhaus, H. B. & Vardoulakis, I. (1987). The thickness of shear bands in granular materials. *Géotechnique* **37**, No. 3, 271–283, doi:10.1680/geot.1987.37.3.271, URL http://www.icevirtuallibrary.com/doi/10.1680/geot.1987.37.3.271.

Muskhelishvili, N. (1977). *Some basic problems of the mathematical theory of elasticity*. Springer science + Business media dordrecht.

Narsilio, G. A. & Santamarina, J. C. (2008). Terminal densities. *Geotechnique* **58**, No. 8, 669–674, doi:10.1680/geot.2008.58.8.669.

Nehari, Z. (1952). *Conformal Mapping*. McGraw-Hill.

Neher, M. (2013). HDD hydrofracture: Roots of the model we use (but don't understand). In *North American Society for Trenchless Technology*.

Oda, M. & Kazama, H. (1998). Microstructure of shear bands and its relation to the mechanisms of dilatancy and failure of dense granular soils. *Géotechnique* **48**, No. 4, 465–481, doi:10.1680/geot.1998.48.4.465, URL http://www.icevirtuallibrary.com/doi/10.1680/geot.1998.48.4.465.

Roscoe, K. H. (1970). The Influence of Strains in Soil Mechanics. *Géotechnique* **20**, No. 2, 129–170, doi:10.1680/geot.1970.20.2.129, URL http://www.icevirtuallibrary.com/doi/10.1680/geot.1970.20.2.129.

Russell, A. R. & Khalili, N. (2006). Cavity Expansion Theory and the Cone Penetration Test in Unsaturated Sands. In *Unsaturated Soils 2006*, Reston, VA: American Society of Civil Engineers, pp. 2546–2557, doi:10.1061/40802(189)217, URL https://doi.org/10.1061/40802(189)217.

Salgado, R., Mitchell, J. K. & Jamiolkowski, M. (1997). Cavity Expansion and Penetration Resistance in Sand. *Journal of Geotechnical and Geoenvironmental Engineering* **123**, No. 4, 344–354, doi:10.1061/(ASCE)1090-0241(1997)123:4(344), URL https://doi.org/10.1061/(ASCE)1090-0241(1997)123:4(344).

Schanz, T. & Vermeer, P. A. (1996). Angles of friction and dilatancy of sand. *Géotechnique* **46**, No. 1, 145–151, doi:10.1680/geot.1996.46.1.145, URL http://www.icevirtuallibrary.com/doi/10.1680/geot.1996.46.1.145.

Stamati, O. (2020). *Impact of meso-scale heterogeneities on the mechanical behaviour of concrete : insights from in-situ x-ray tomography and E-FEM modelling*. Theses, Université Grenoble Alpes [2020-....], URL https://tel.archives-ouvertes.fr/tel-02923399.

Stamati, O., Andò, E., Roubin, E., Cailletaud, R., Wiebicke, M., Pinzon, G., Couture, C., Hurley, R. C., Caulk, R., Caillerie, D. *et al.* (2020). spam: Software for practical analysis of materials. *Journal of Open Source Software* **5**, No. 51, 2286.

Terzaghi, K., Peck, R. B. & Mesri, G. (1996). *Soil Mechanics in Engineering Practice*. 3rd edn., Wiley, doi:10.1097/00010694-194911000-00029, URL https://insights.ovid.com/crossref?an=00010694-194911000-00029.

Tien, H.-j. (1996). *A Literature Study of the Arching Effect*. Ph.D. thesis, Massachusetts Institute of Technology.

Timoshenko, S. F. & Goodier, J. N. (1951). *Theory of Elasticity*. Second edi edn., McGraw-Hill.

Vermeer, P. A. (1990). The orientation of shear bands in biaxial tests. *Geotechnique* **40**, No. 2, 223–236, doi:10.1680/geot.1990.40.2.223, URL http://www.icevirtuallibrary.com/doi/10.1680/geot.1990.40.2.223.

White, D. J., Barefoot, A. J. & Bolton, M. D. (2001). Centrifuge modelling of upheaval buckling in sand. *International Journal of Physical Modelling in Geotechnics* **1**, No. 2, 19–28, doi:10.1680/ijpmg.2001.010202, URL http://www.icevirtuallibrary.com/doi/10.1680/ijpmg.2001.010202.

White, D. J., Cheuk, C. Y. & Bolton, M. D. (2008). The uplift resistance of pipes and plate anchors buried in sand. *Geotechnique* **58**, No. 10, 771–779, doi:10.1680/geot.2008.3692.

Wong, K., Ng, C., Chen, Y. & Bian, X. (2012). Centrifuge and numerical investigation of passive failure of tunnel face in sand. *Tunnelling and Underground Space Technology* **28**, No. 1, 297–303, doi:10.1016/j.tust.2011.12.004, URL https://linkinghub.elsevier.com/retrieve/pii/S088677981100160X.

Wong, R. C. K. & Kaiser, P. K. (1991). Performance Assessment of Tunnels in Cohesionless Soils. *Journal of Geotechnical Engineering* **117**, No. 12, 1880–1901, doi:10.1061/(ASCE)0733-9410(1991)117:12(1880), URL https://doi.org/10.1061/(ASCE)0733-9410(1991)117:12(1880).

Wood, D. M. (1990). Strain-dependent mduli and pressuremeter tests. *Géotechnique* **40**, No. 3, 509–512, doi:10.1680/geot.1990.40.3.509, URL http://www.icevirtuallibrary.com/doi/10.1680/geot.1990.40.3.509.

Xia, H. W. & Moore, I. D. (2006). Estimation of maximum mud pressure in purely cohesive material during directional drilling. *Geomechanics and Geoengineering* **1**, No. 1, 3–11, doi:10.1080/17486020600604024, URL http://www.tandfonline.com/doi/abs/10.1080/17486020600604024.

Yang, Y. & Yu, H. (2010). Finite element analysis of anchor plates using non-coaxial models. *Journal of Rock Mechanics and Geotechnical Engineering* **2**, No. 2, 178–187, doi:10.3724/SP.J.1235.2010.00178.

Yu, H.-S. (2000). *Cavity Expansion Methods in Geomechanics*. Dordrecht: Springer Netherlands, doi:10.1007/978-94-015-9596-4, URL http://link.springer.com/10.1007/978-94-015-9596-4.

Zhang, R. & Yang, X. (2018). Limit analysis of active and passive mechanisms of shallow tunnels in nonassociative soil with changing water table. *International Journal of Geomechanics* **18**, No. 7, 1–13, doi:10.1061/(ASCE)GM.1943-5622.0001167.

Zhao, L. h., Tan, Y. g., Hu, S. h., Deng, D. p. & Yang, X. p. (2018). Upper bound analysis of ultimate pullout capacity of shallow 3-D circular plate anchors based on nonlinear Mohr-Coulomb failure criterion. *Journal of Central South University* **25**, No. 9, 2272–2288, doi:10.1007/s11771-018-3912-7.

Zhou, H., Kong, G. Q. & Liu, H. L. (2016). Pressure-controlled elliptical cavity expansion under anisotropic initial stress: Elastic solution and its application. *Science China Technological Sciences* **59**, No. 7, 1100–1119, doi:10.1007/s11431-016-6023-4, URL http://link.springer.com/10.1007/s11431-016-6023-4.

Zou, J., Chen, G. & Qian, Z. (2019). Tunnel face stability in cohesion-frictional soils considering the soil arching effect by improved failure models. *Computers and Geotechnics* **106**, 1–17, doi:10.1016/j.compgeo.2018.10.014.